Electronic Supplementary Material (ESI) for Materials Horizons.

Supporting Information

for

Heterogeneous CNF/MoO_3 Nanofluidic Membranes with Tunable Surface Plasmon Resonances for Solar-Osmotic Energy Conversion

This PDF file includes:

Supporting Notes 1-6

Supporting Figures 1-24

Supporting Table 1

Supporting Note 1| Preparation of Amorphous MoO_3 nanosheets

The typical process was as followed. MoS_2 (100 mg) was dispersed in an aqueous solution (10 mL) with 45% ethanol volume fraction and ultrasound for 4h to form a uniform solution. It was then dried in a constant temperature oven at 60° C MoO_3 was prepared by annealing the pre-treated MoS_2 at 350° C for 90 min. The resulting MoO_3 was dispersed in a 45% ethanol/water mixture (10 ml) followed by ultrasound for 60 minutes to achieve good dispersion. The dispersion was then quickly transferred to a SC-CO_2 unit, which consisted primarily of a stainless-steel autoclave with a heating jacket and temperature controller. The autoclave was heated to 80° C and CO_2 was filled into the reactor to the required pressure (20 MPa). After 3h reaction, CO_2 was released slowly. The dispersion was then centrifuged at 6000 rpm for 15 min, the aggregates were removed at room temperature, and the supernatant was collected.

Supporting Note 2| Preparation of heterogeneous nanofluidic membranes

The CNF solution (2 mL, 1 mg/mL) was filtered for 45 min, and then the according MoO_3 solution 2 mL, 1 mg/mL, MoO_3: Ultrasonicated treated; $MoO_{3(SC)}$: SC-CO_2 treated; $MoO_{3(SC\text{-}L12)}$: Light irradiation for 12 minutes after SC-CO_2 treatment and immediately filtered for another 2 hours to form the heterogeneous nanofluidic composite membranes.

Supporting Note 3 |The intercalation mechanism

The intercalation process can be expressed as follows:[1]

$$MoO_3 \rightarrow MoO_3^* + h^+ + e^- \quad (1)$$

$$2h^{+} + H_2O \rightarrow 2H^{+} + \frac{1}{2}O_2 \quad (2)$$

$$MoO_3 + xH^{+} + xe^{-} \rightarrow H_xMoO_3 \quad (3)$$

Supporting Note 4| Electrode calibration

The energy conversion property is analyzed by scanning the I−V cycles in the presence of a concentration gradient across the membrane. The sweeping voltages from -0.2 V to 0.2 V are applied with a step of 0.02V. The intercept on the voltage axis (V_{oc}) is caused by E_{redox} and E_{diff}. In this work, the value of E_{redox} was measured using an experimental method. The electrode calibration is operated in the same electrochemical cell without membrane to measured voltages. In this case, the measured potential was contributed solely by the asymmetric redox reactions on the electrodes (E_{redox}). The electrode potential remained stable during the calibration process as the diffusion of ions did not affect the bulk concentration obviously in the first several minutes. Such an experimental method can largely preclude the influence brought by many unexpected factors such as the contamination and electrode imperfection. The obtained V_{oc}, E_{redox} and E_{diff} are summarized in Table S1.

Supporting Note 5 | Density functional theory (DFT) simulations

Density functional theory (DFT) simulations were performed by the CP2K software package.[2, 3] The Gaussian plane wave (GPW) method,[4] which combines the double-zeta-polarized Gaussian basis optimized for condensed systems and the plane-wave basis set (with an energy cutoff of 400 Ry), was employed to efficiently solve the DFT

Kohn-Sham equation. Additionally, the ion-electron interaction was accounted for using the GTH norm-conserving pseudopotential.[5, 6] All structures were thoroughly optimized using the Broyden-Fletcher-Goldfarb-Shanno (BFGS) minimization algorithm,[7, 8] the geometry change was converged within 3E-3 Bohr, the root mean square (RMS) of geometry change was converged within 1.5E-3 Bohr, the force was converged within 4.5E-4 Bohr/Hartree, and the RMS of force was converged within 3E-4 Bohr/Hartree. The selection of the exchange-correlation functional plays a pivotal role in determining the precision of the simulation. Consequently, for tasks such as structural optimization and molecular dynamics simulations, the meta-GGA R^2SCAN functional[9] in conjunction with the DFT-D3 dispersion correction scheme[10] was employed. This approach is recognized for its ability to accurately determine the structure of transition metal oxides. Furthermore, the use of hybrid functionals is essential for deriving reliable electronic structures of transition metal oxides. As such, the B3LYP functional[9, 11] was utilized to calculate the electronic state density and electronic excitations. In addition, the study of excited states was accelerated by the Tamm-Dancoff approximation[8, 12-14] The excited state energy produced by this method is essentially the same as that obtained from the time-dependent density functional theory itself, when the same exchange-correlation functional is used.

In this research, a melt-quench scheme, underpinned by molecular dynamics simulations, was used to generate amorphous structures. Specifically, the initial crystal structure was subjected to complete melting at a temperature of 2500 K, yielding a high-temperature amorphous structure. This structure was subsequently cooled to 300 K,

resulting in a room-temperature amorphous structure following comprehensive equilibrium. Throughout the series of molecular dynamics simulations, the Canonical Sampling through Velocity-Rescaling (CSVR) thermostat[15] was employed to establish the canonical ensemble, operating with a time step of 1 fs. The radial distribution function (RDF) showed that the atomic arrangement of the final structure has typical short-range ordered and long-range disordered amorphous characteristics.

Supporting Note 6 | Numerical simulation

The thermoelectric conversion phenomenon was theoretically investigated using commercial finite-element software package COMSOL (version 5.4; COMSOL Inc., Stockholm, Sweden) Multiphysics based on "electrostatics (Poisson equation)" and "Nernst-Planck without Electroneutrality" modules. The coupled governing Poisson and Nernst-Planck (PNP) Equations are shown as below:

$$J_i = D_i\left(\nabla c_i + \frac{z_i F c_i}{RT}\nabla\varphi\right) + c_i u \tag{4}$$

$$\nabla^2\varphi = -\frac{F}{\varepsilon}\sum z_i c_i \tag{5}$$

$$\nabla \cdot J_i = 0 \tag{6}$$

Here, the physical quantities J_i, D_i, c_i, φ, u, R, F, T, and ε refer to the ionic flux, diffusion coefficient, ion concentration, electrical potential, fluid velocity, universal gas constant, Faraday constant, absolute temperature, and dielectric constant of the electrolyte solutions, respectively. The equation (4) is the Nernst–Planck equation which describes the transport property of a charged nanochannel. Equation (5) is the Poisson equation which describes the relationship between the electrical potential and ion concentrations. Besides, the flux should satisfy the time-independent continuity equation (6) when the

system reaches a stationary regime. A simplified negatively charged ($\sigma = -0.01$ C/m^2 and -0.015 C/m^2) channel was chosen as the simulated model. To carry out the calculations, the "electrostatics (AC/DC)" and "Nernst-Plank without electroneutrality" modules were used. In addition, to precisely set the temperature of the channel, the "heat transfer in fluids" module was coupled to this model. The model with a temperature difference of 30 K (room temperature is set to 298 K) was applied. The coupled equations (4-6) must be solved for a given geometry using appropriate boundary conditions.

The boundary condition for the potential φ on the channel wall is

$$\vec{n} \cdot \nabla\varphi = -\frac{\sigma}{\varepsilon} \tag{7}$$

The ion flux has zero normal components at the bound aries:

$$\vec{n} \cdot J = 0 \tag{8}$$

The parameter σ (σ is set to −0.01 C/m^2 and -0.015 C/m^2) is the surface charge density of the channel walls. Then, the ionic current can be calculated by:

$$I = \int sF(Z_p j_p + Z_n j_n) \cdot \vec{n}\, ds \tag{9}$$

Supporting Figures

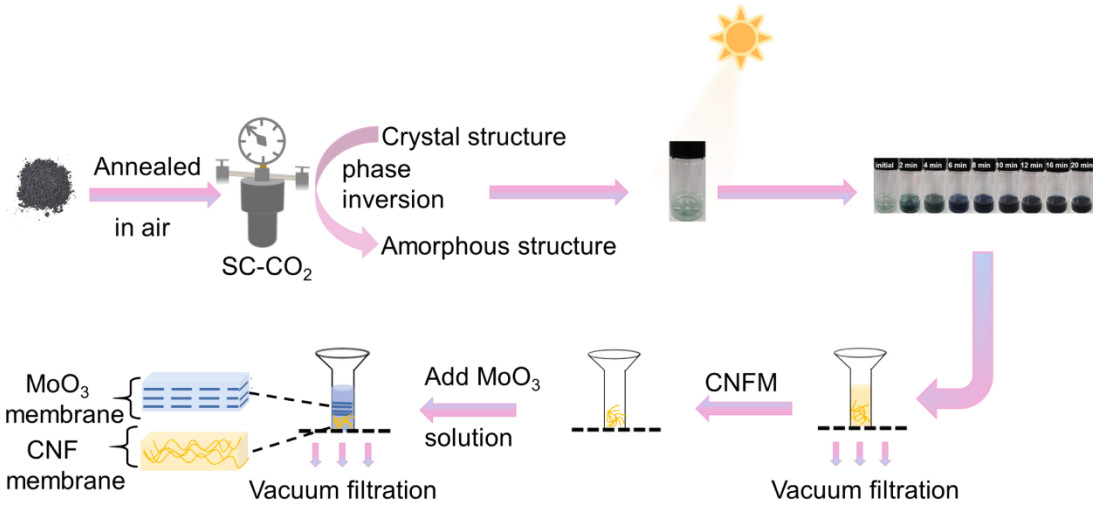

Figure S1. Preparation of amorphous MoO_3 and heterogeneous nanofluidic membranes.

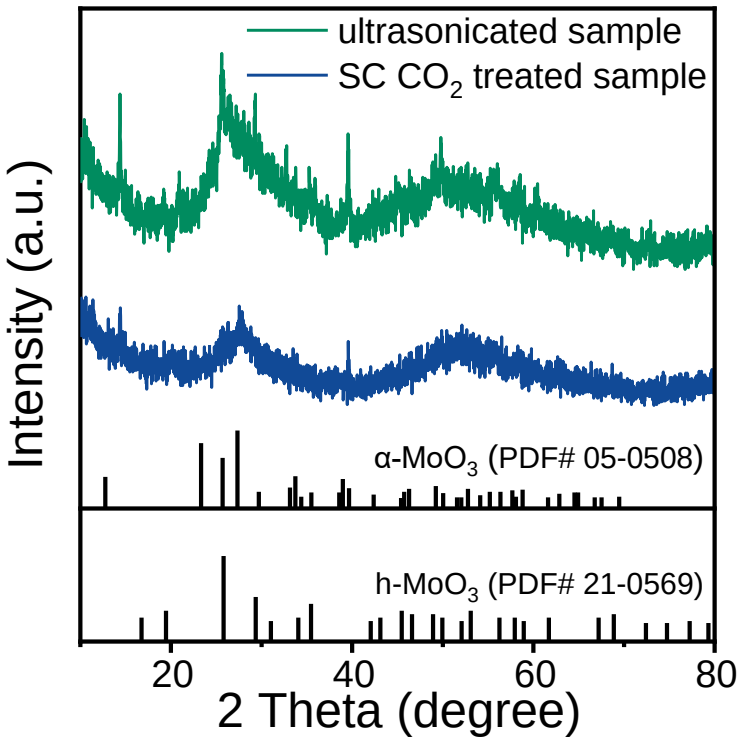

Figure S2. X-Ray Diffraction (XRD) patterns of 2D MoO_3 flakes illustrating that SC-CO_2 treated MoO_3 nanosheets were amorphous body. XRD patterns at the bottom show h-MoO_3 (PDF# 21-0569) and α-MoO_3 (PDF# 05-0508).

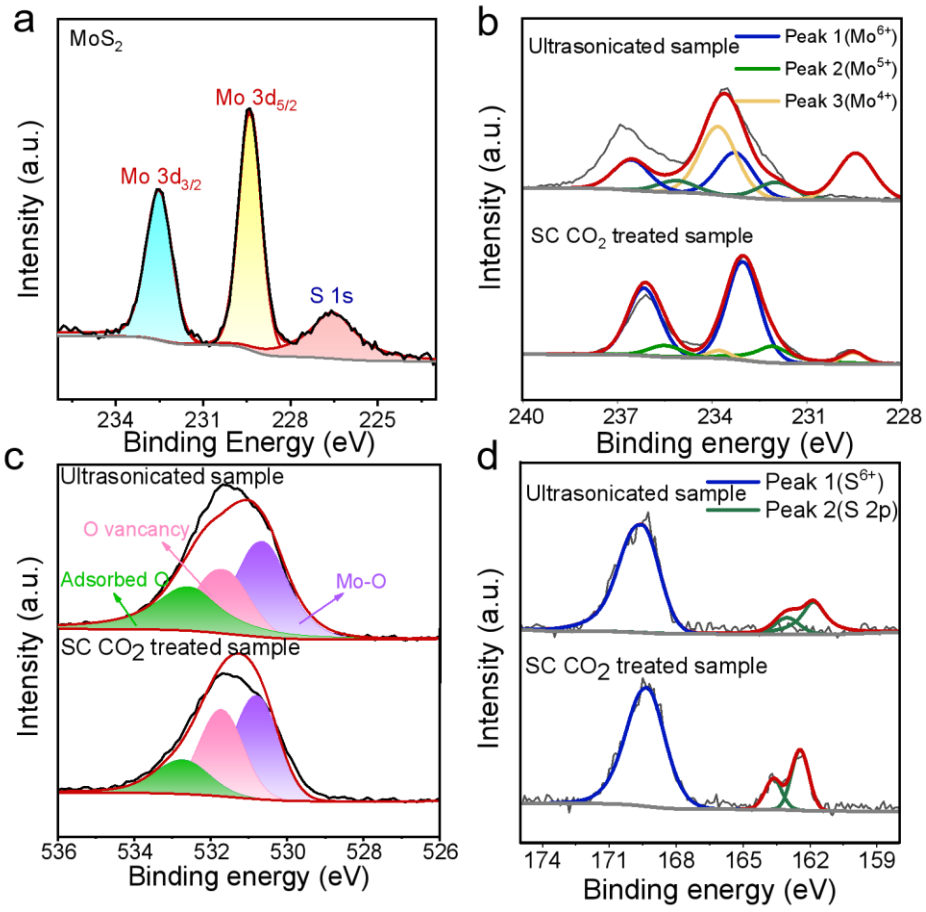

Figure S3. (a) XPS spectra of MoS_2 powder. (b) In the high resolution XPS spectrum for Mo 3d, there are mainly three kinds of Mo atoms composed of Mo 3d, which are Mo^{6+} (236.5 and 233.8 eV), Mo^{5+} (235.1 and 231.9 eV), and Mo^{4+} (233.8 and 229 eV), respectively. The SC-CO_2 treated MoO_3 nanosheets contains a high concentration of the Mo^{6+}, indicating that the SC-CO_2 treated sample was oxidized more completely. (c) In the high resolution XPS spectrum for O 1s. This experimental data clarifies the 2D amorphous MoO_3 nanosheets contain largely oxygen vacancies compared to the ultrasonicated sample[16] and (d) The high resolution of O 1s can be deconvoluted into three peaks, corresponding to lattice oxygen (530.6 eV), oxygen vacancies (531.7 eV), and surface adsorbed species (532.6 eV), respectively. The weak peaks at 163.6 and 161.8 eV can be assigned to S^{2-} $2p_{3/2}$ and S^{2-} $2p_{1/2}$. Whereas the strong peaks at 169.3

eV is corresponding to + 6 oxidation state of sulfur, which results from the oxidation of divalent sulfide ions.

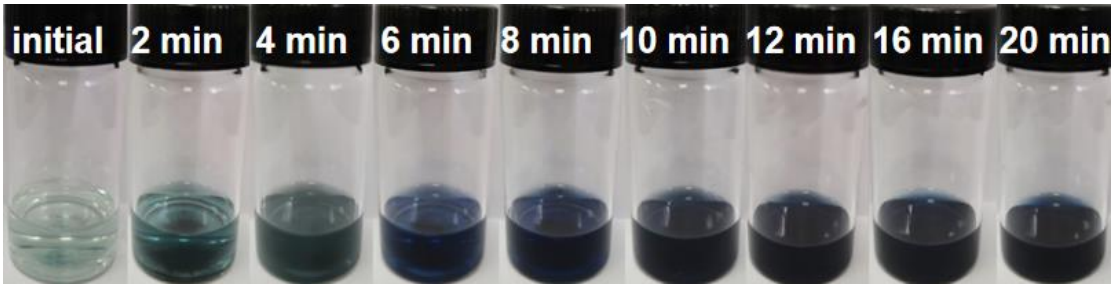

Figure S4. Photograph of the 2D amorphous nanosheets suspensions at different Xenon lamp with a power of 1.3 W/cm^2.

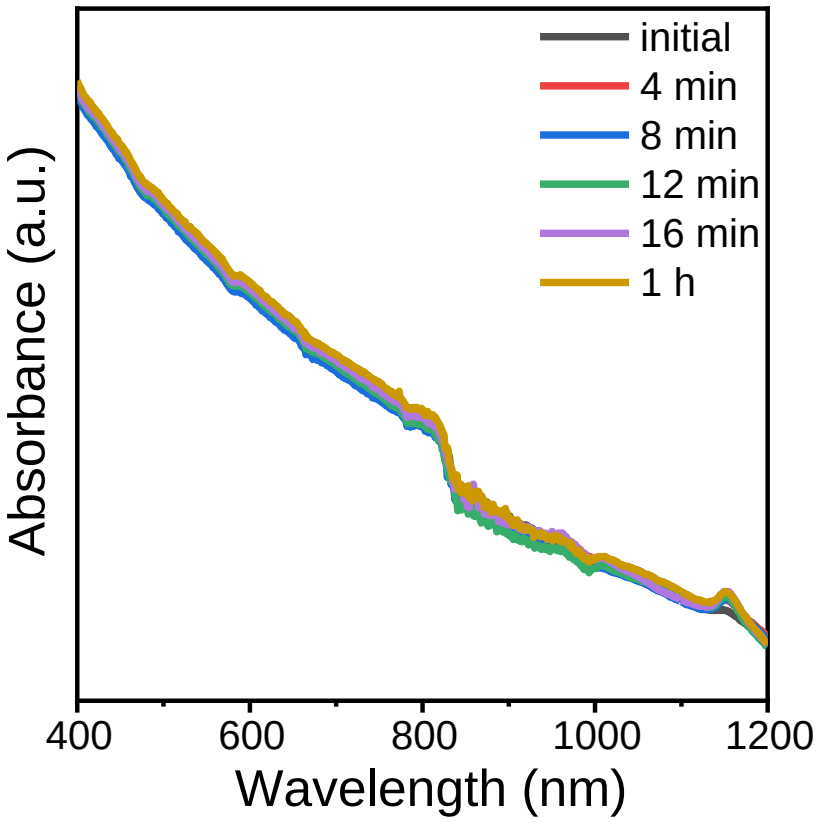

Figure S5. Vis-NIR absorbance spectra of the CNF solution with and without irradiation with a Xenon lamp with a power of 1.3 W/cm^2.

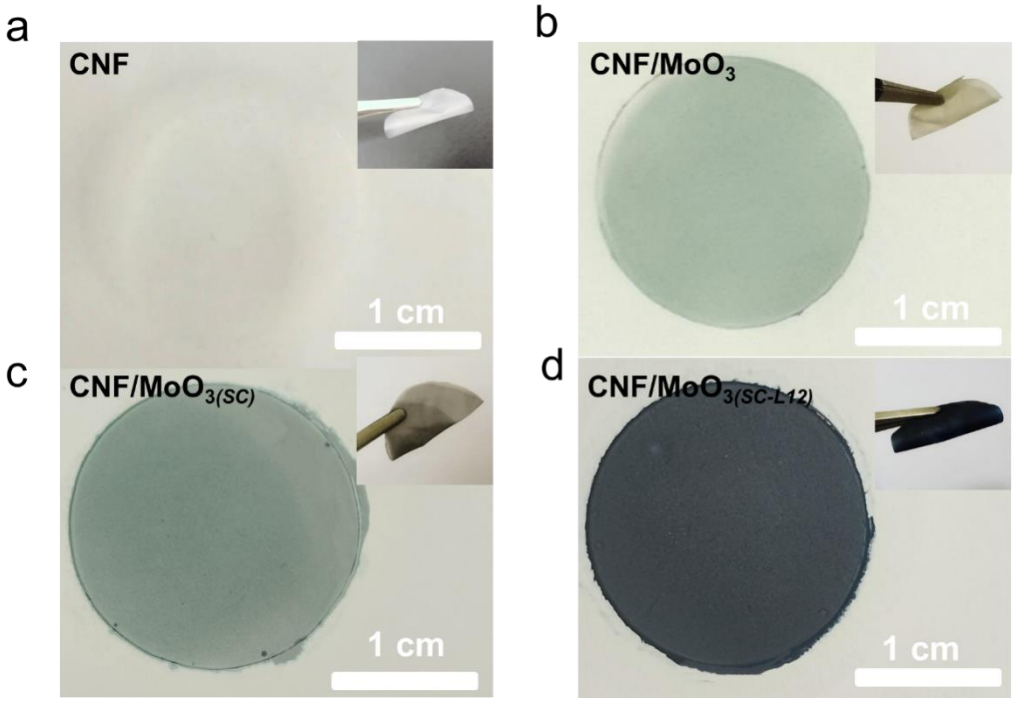

Figure S6. Photograph of four self-supporting and flexible membranes. (a) CNF membrane, (b) CNF/MoO_3 composite membrane, (c) $CNF/MoO_{3(SC)}$ composite membrane and (d) $CNF/MoO_{3(SC\text{-}L12)}$ composite membrane.

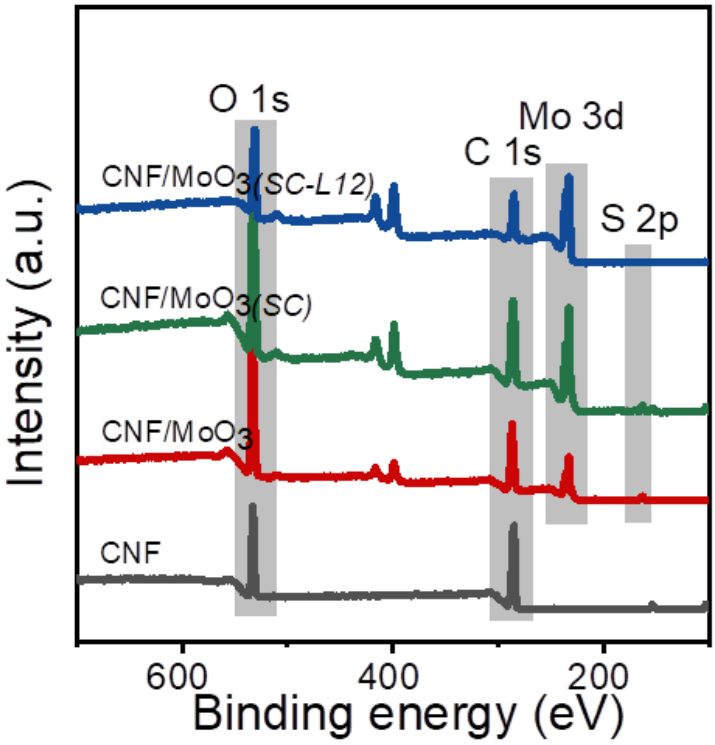

Figure S7. XPS spectra of four membranes: fully scanned XPS spectrum.

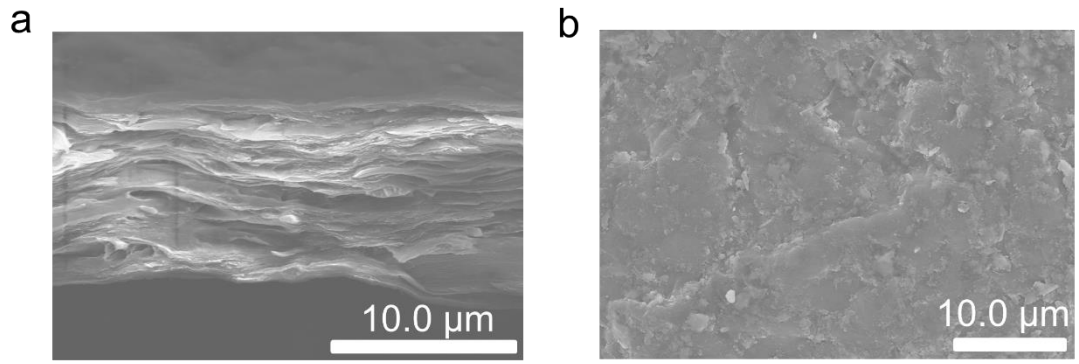

Figure S8. (a) Cross sectional SEM image of the CNF/MoO_3 composite membrane, showing an ordered lamellar structure. (b) SEM cross-sectional image of this composite membrane.

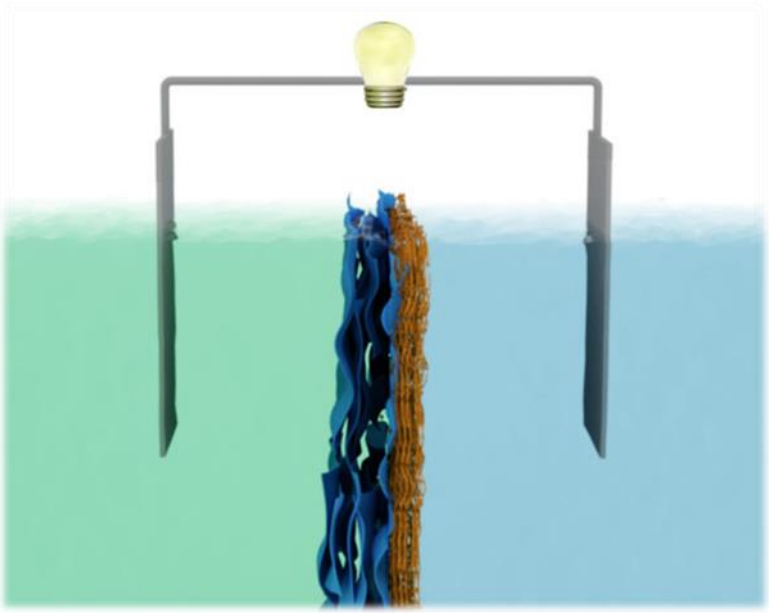

Figure S9. Experimental device for energy conversion under salinity gradient. A pair of homemade Ag/AgCl electrodes is employed to measure the ionic currents.

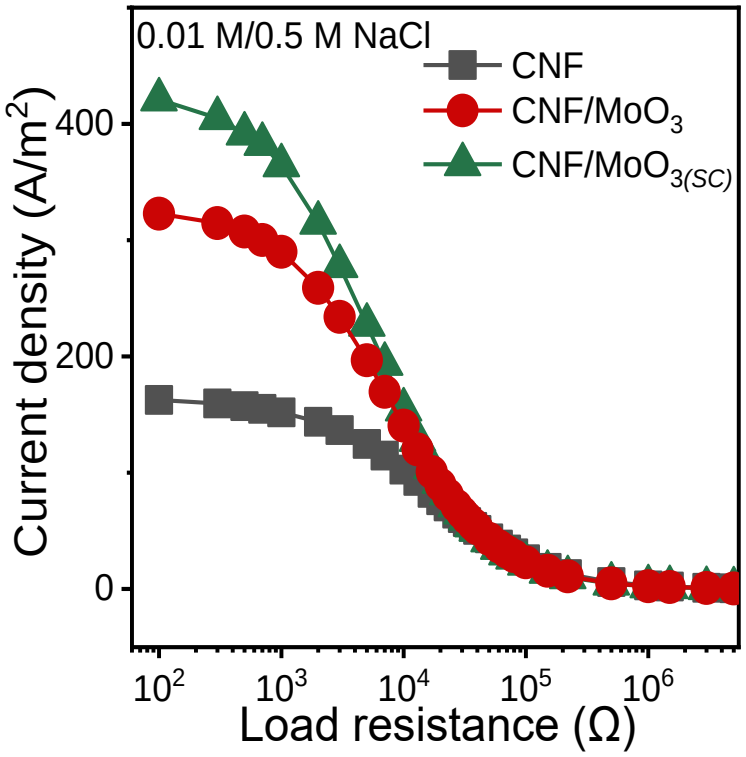

Figure S10. Recorded current density of three membranes as a function of the load resistances (R_L) in the experiment.

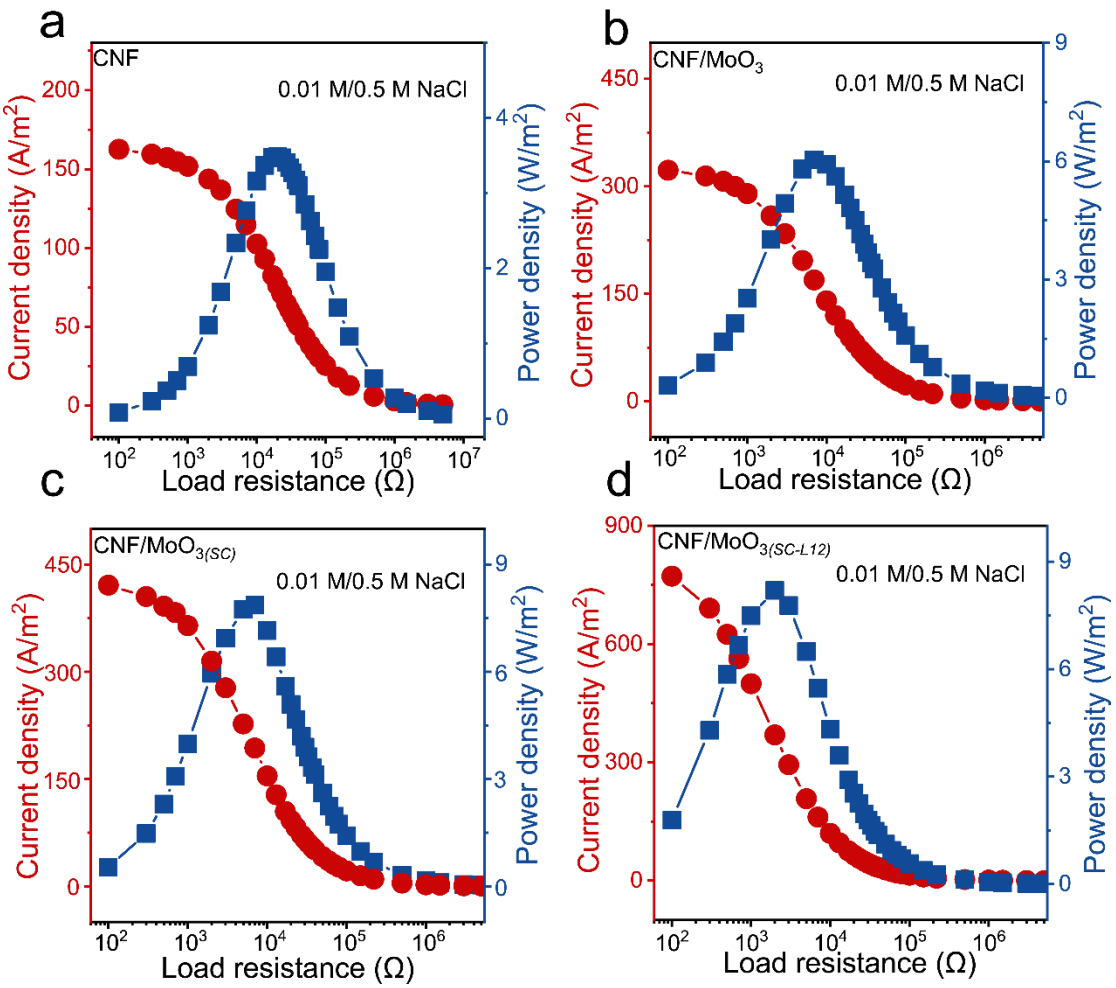

Figure S11. Output power density and current density as the functions of R_L under a 50-fold concentration gradient. The output power density reaching a peak value of (a) 3.49 W/m^2, (b) 6.04 W/m^2, (c) 7.86 W/m^2, (d) 9.07 W/m^2, respectively.

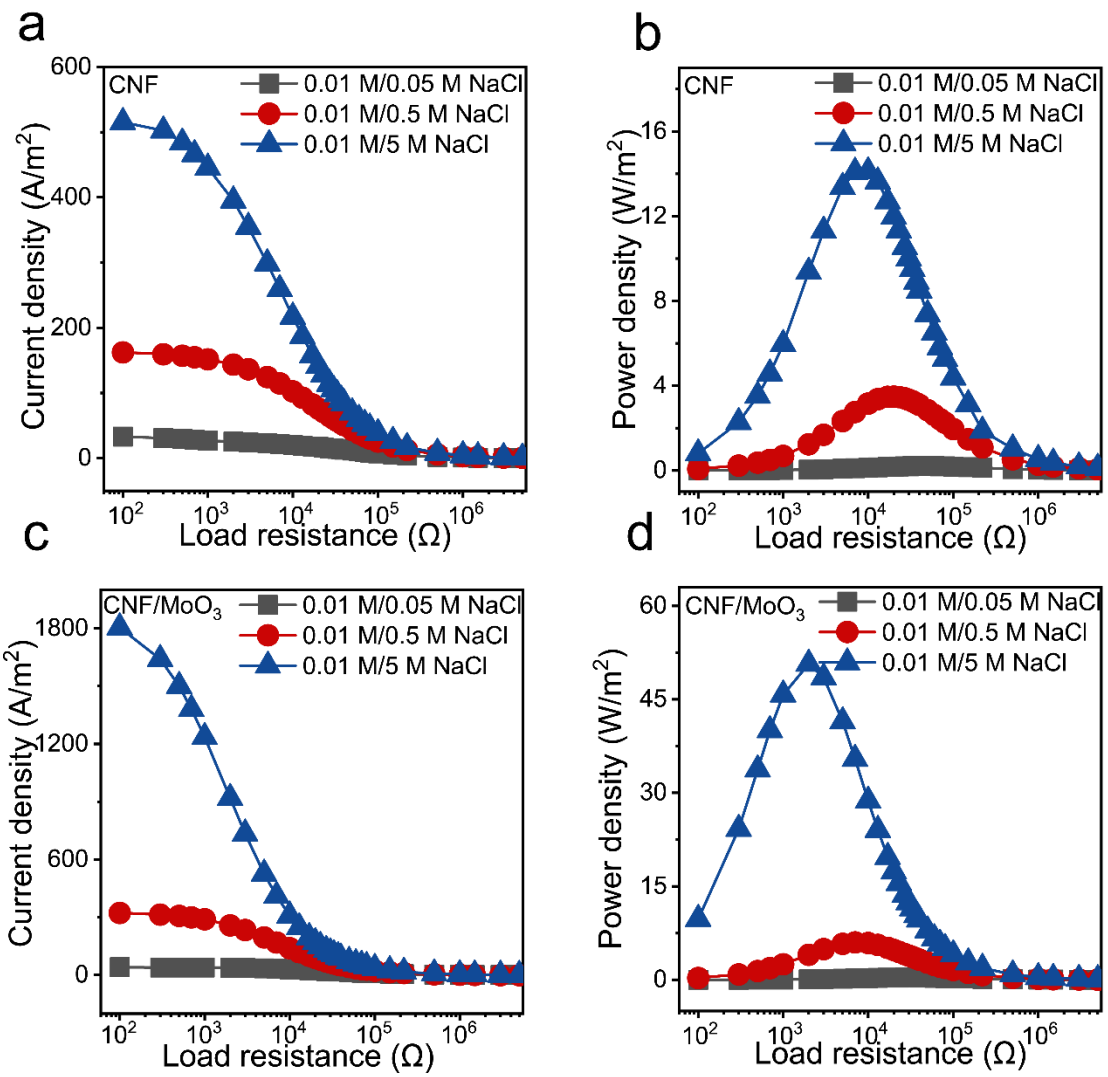

Figure S12. Output power density and current density as the functions of R_L under three concentration gradients (5, 50, 500) of (a-b) CNF membrane and (c-d) CNF/MoO_3 composite membrane.

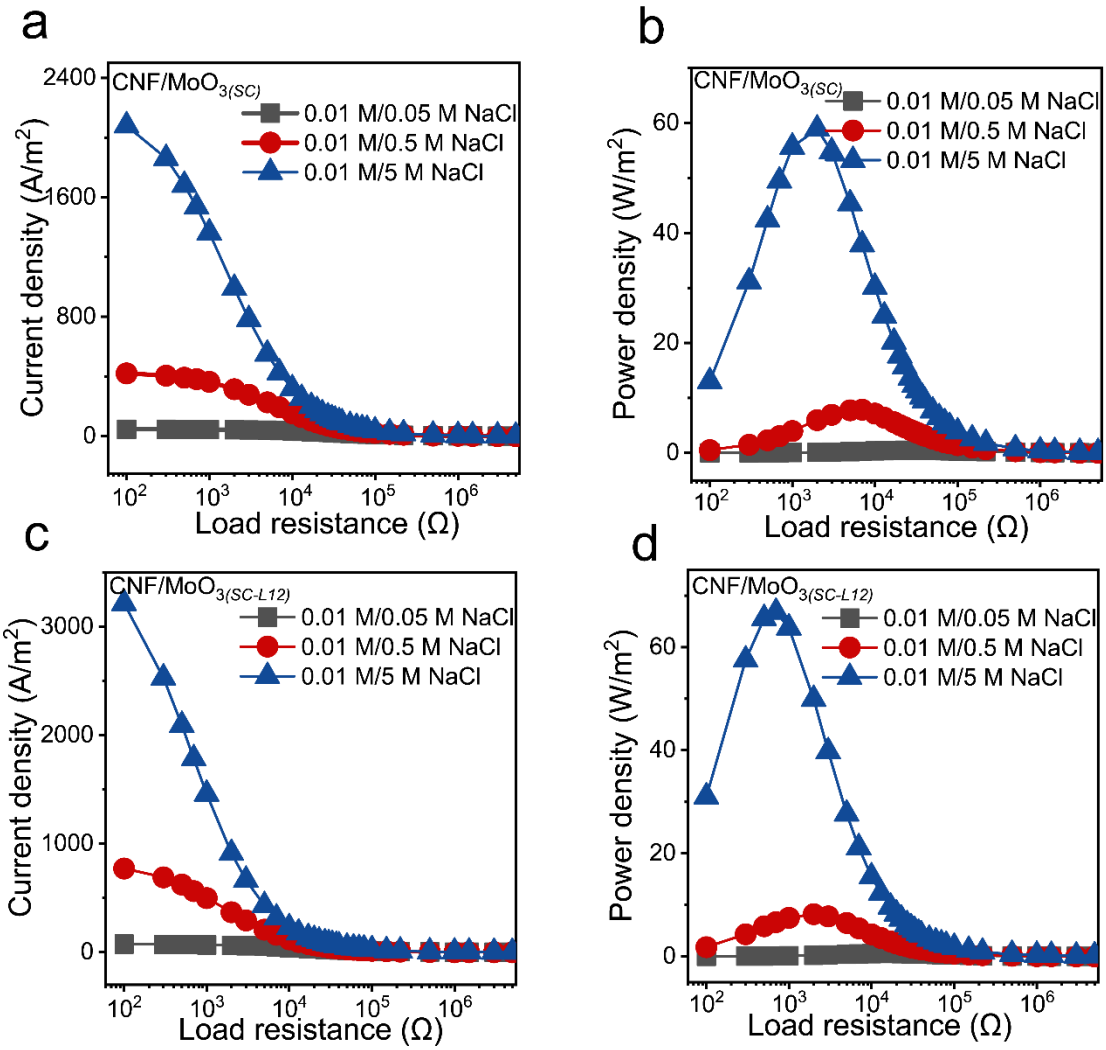

Figure S13. Output power density and current density as the functions of R_L under three concentration gradients (5, 50, 500) of (a-b) $CNF/MoO_{3(SC)}$ composite membrane and (c-d) $CNF/MoO_{3(SC-L12)}$ composite membrane.

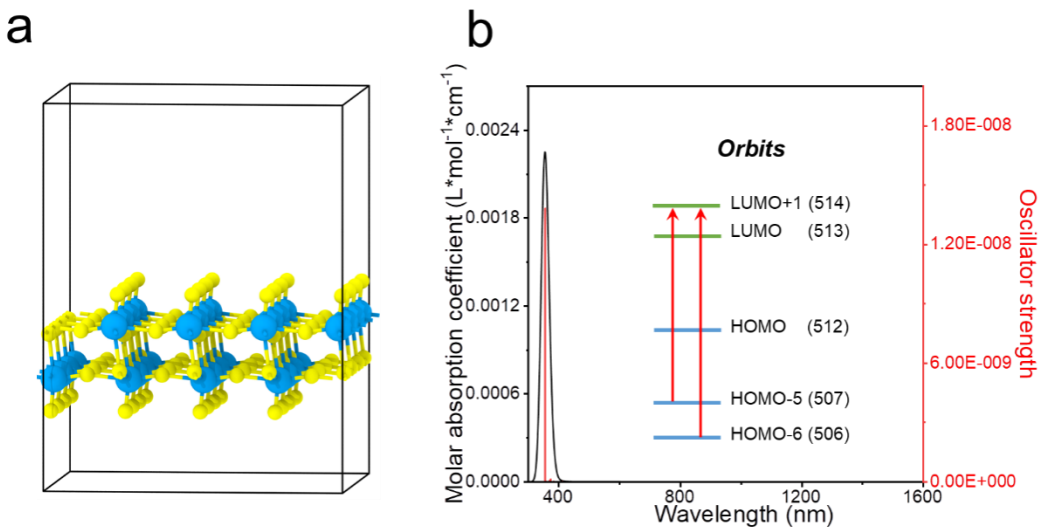

Figure S14. (a) Single layer crystal MoO_3 surface model and (b) light absorption spectrum and excitation analysis of crystal MoO_3 based on DFT.

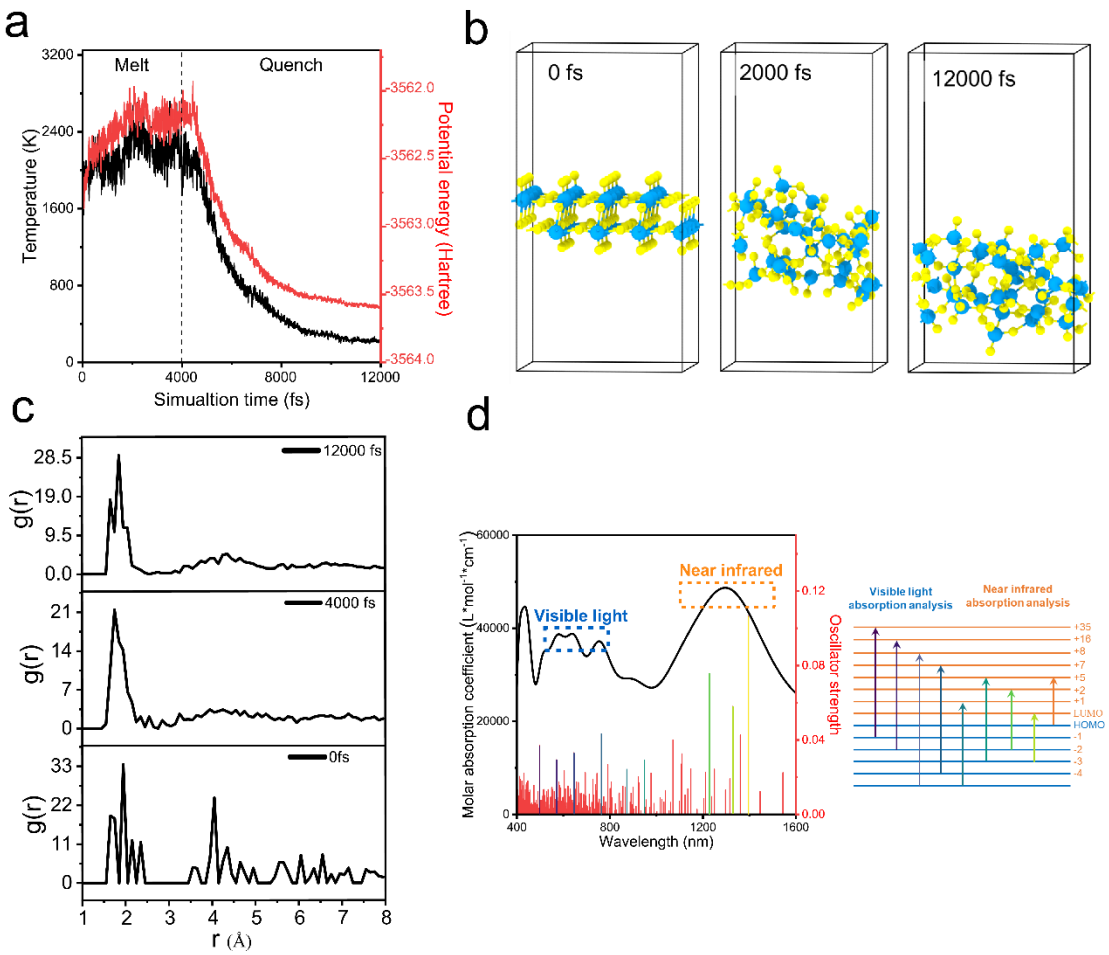

Figure S15. (a) Kinetic and potential energy evolution in the melt-quench simulation of amorphous $MoO_{2.7}$, (b) side view of the structure at different time stages, (c) RDF of the structure at different time stages, (d) light absorption spectrum and excitation analysis of amorphous $MoO_{2.7}$.

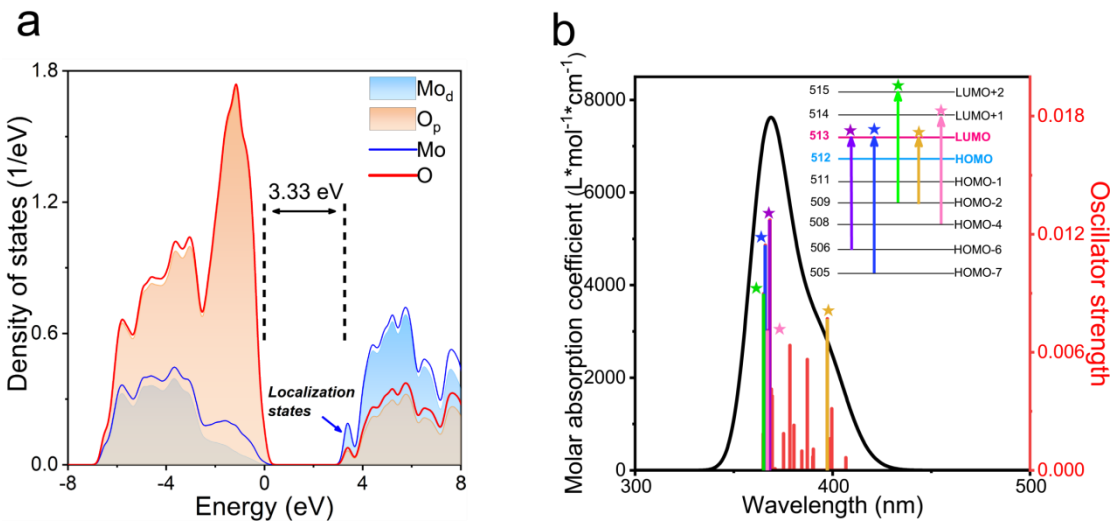

Figure S16. (a) Calculated DOS of amorphous MoO_3., (b) light absorption spectrum and excitation analysis of amorphous MoO_3.

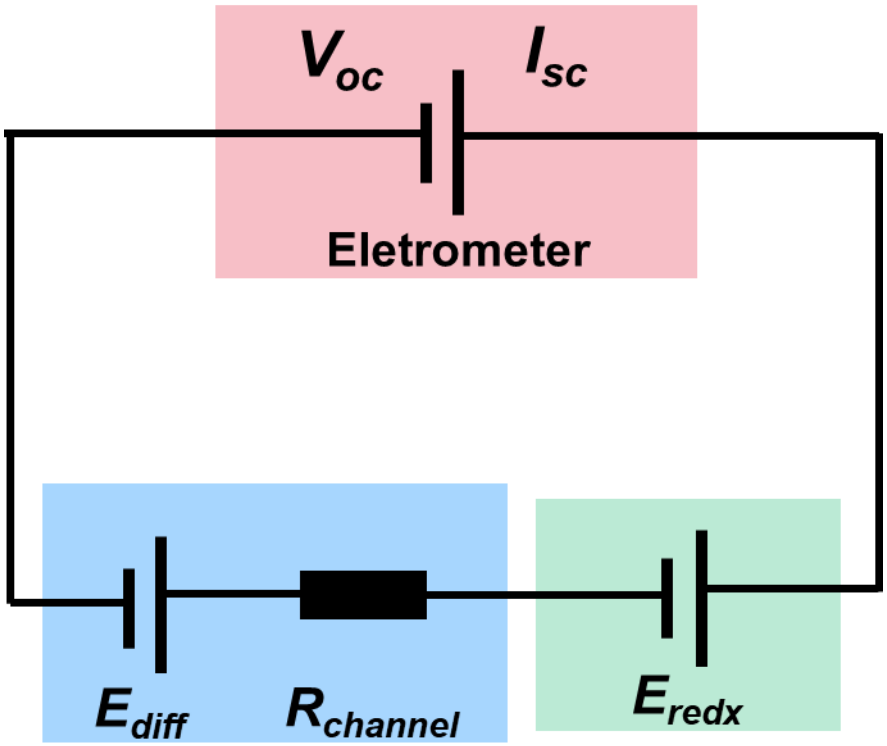

Figure S17. Equivalent circuit diagram of the power source. The measured V_{OC} is composed of diffusion potential (E_{diff}) and redox potential (E_{redox}). E_{diff} can be calculated as: $E_{diff} = V_{OC} - E_{redox}$.

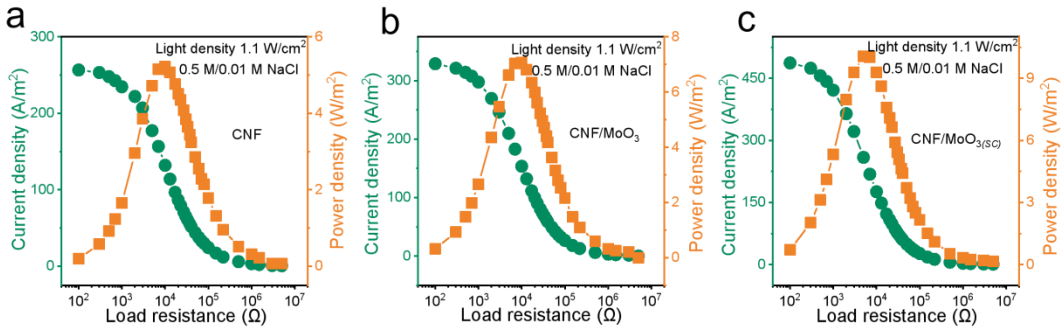

Figure S18. The output power density and current density after illumination are functions of the R_L. The output power density reaching a peak value of (a) 4.64 W/m^2, (b) 7.07 W/m^2, (c) 10.01 W/m^2, respectively.

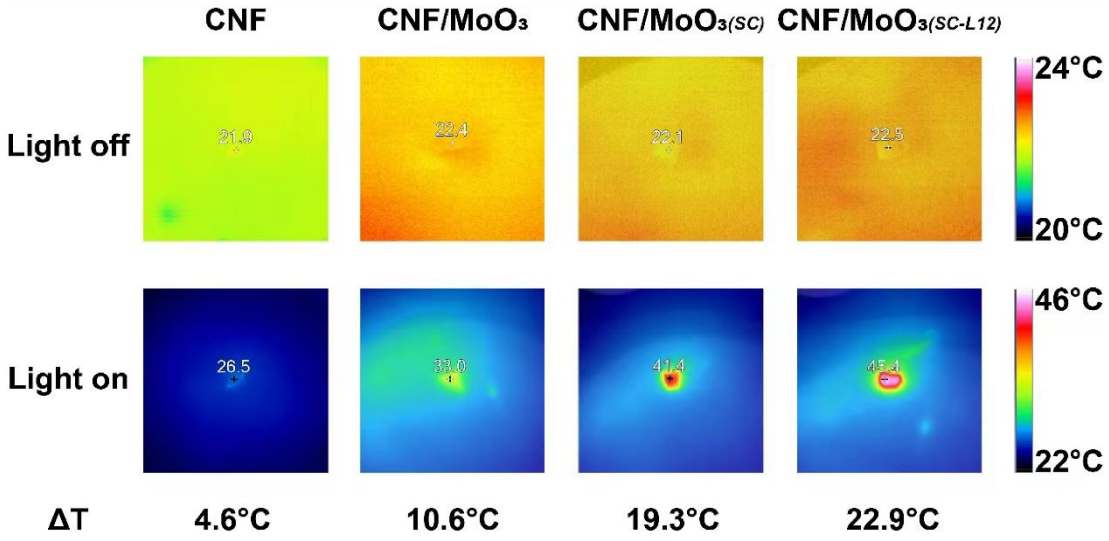

Figure S19. IR camera images CNF pure membrane and CNF/MoO_3, CNF/$MoO_{3(SC)}$ and CNF/$MoO_{3(SC-L12)}$ heterogeneous nanofluidic membranes with and without light illumination.

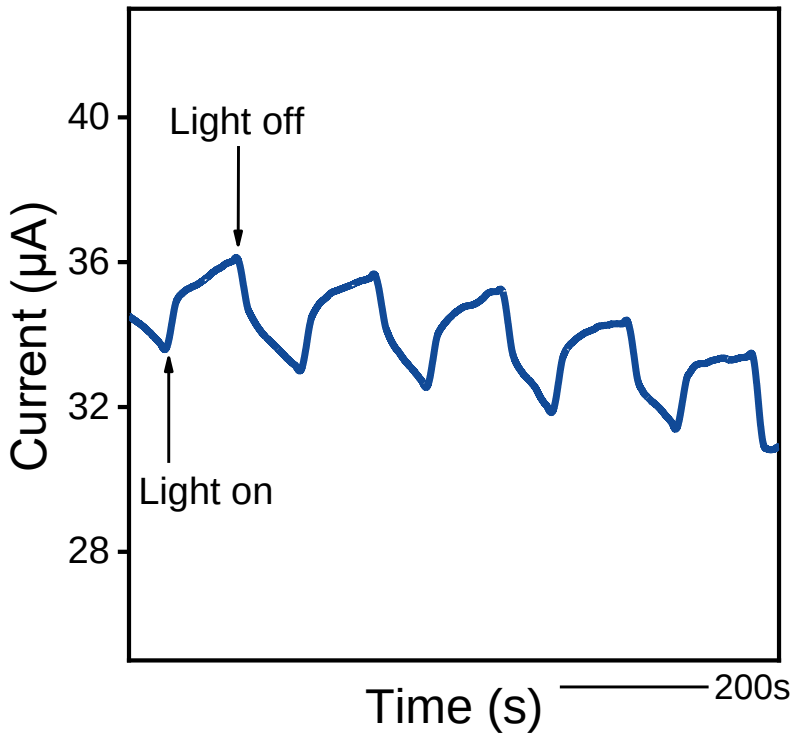

Figure S20. Current-time curve obtained in the photo "On-Off" experiment.

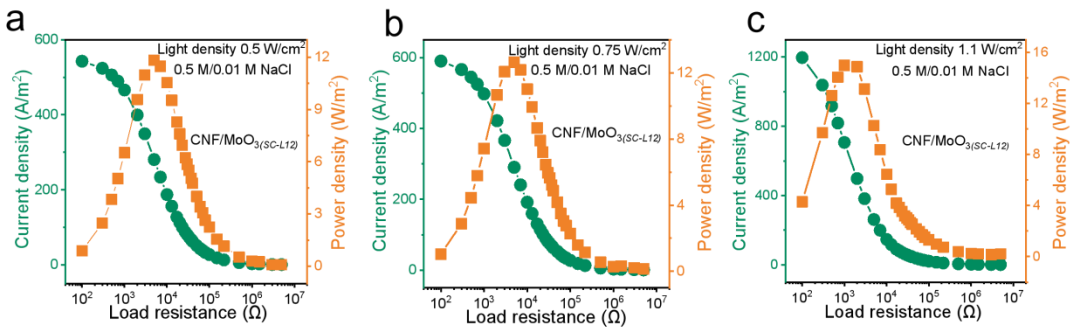

Figure S21. Output power density and current density at different light density as the functions of load resistances under a 50-fold concentration gradient. The output power density reaching a peak value of (a) 11.48 W/m^2, (b) 12.64 W/m^2, (c) 13.24 W/m^2, respectively.

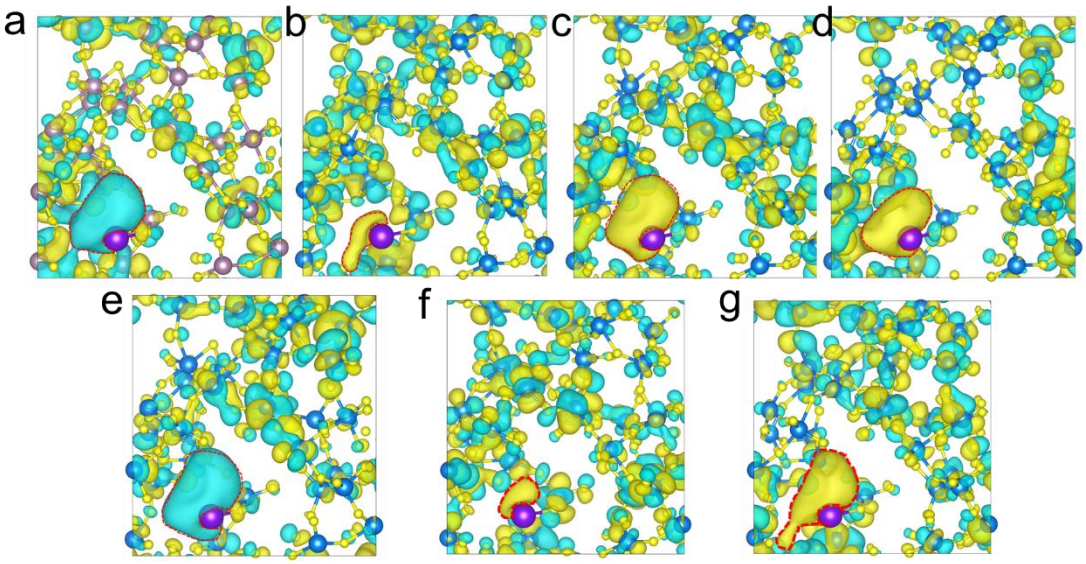

Figure S22. Excited-state electron spatial distributions at different excitation energy (a-e: 1.006 eV; f-g: 1.993 eV purple ball: Na^+, yellow and cyan: excited state electrons).

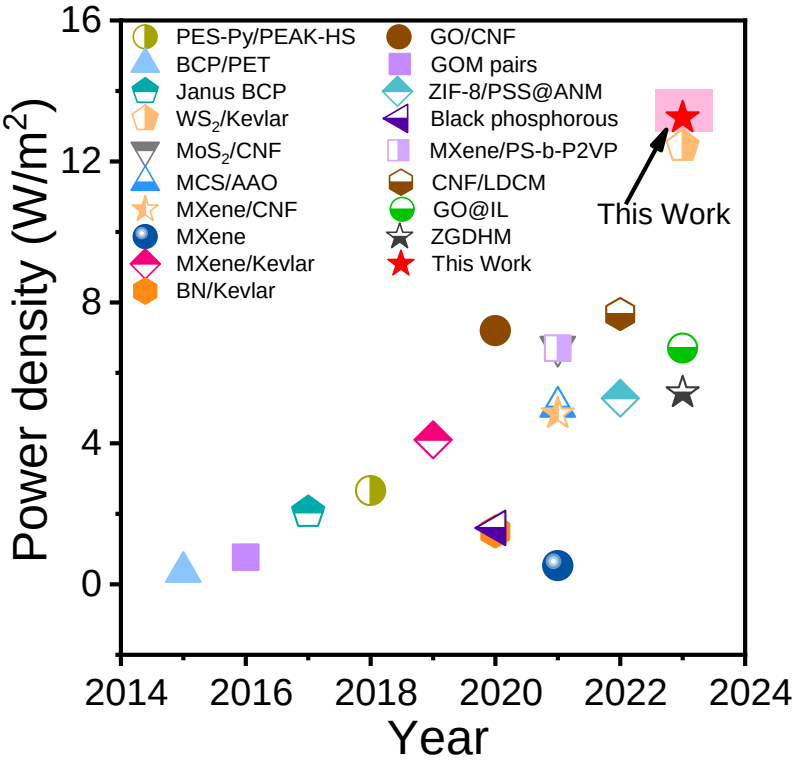

Figure S23. Comparison of the power density under 50-fold concentration gradient with the reported membrane-based systems in the literature under the same testing area.[17-26]

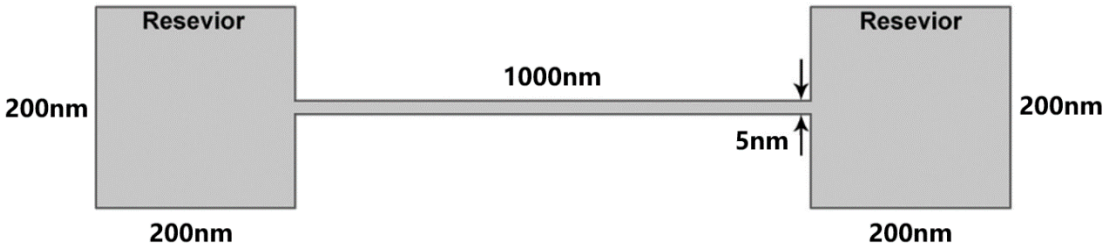

Figure S24. Numerical simulation model (Drawing not to scale).

Membranes	CNF			CNF/MoO_3			CNF/$MoO_{3(SC)}$			CNF/$MoO_{3(SC-L12)}$		
C_H/C_L	5	50	500	5	50	500	5	50	500	5	50	500
V_{oc} (mV)	38.62	73.71	107.64	40.74	72.21	108.11	51.13	74.84	108.76	52.57	86.94	111.94
E_{redx} (mV)	13.26	15.29	22.16	13.29	15.29	22.16	13.26	15.29	22.16	13.26	15.29	22.16
E_{diff} (mV)	25.36	58.42	85.48	27.45	56.92	85.95	37.87	59.55	86.60	39.31	71.65	89.78

Table S1. V_{oc} and E_{redox} of membranes under corresponding concentration gradient. Diffusion potential (E_{diff}) can be calculated via an electrode calibration process that substrates the contribution of redox potential (E_{redox}) generated by the unequal potential drop at the electrode-solution interface. The E_{diff} can be described as: $E_{diff} = V_{oc} - E_{redox}$.

References

[1] L. Wei, X. Qun, C. Weili, Z. Chuanhui, Q. Yuhang, *Angew Chem* **2017**, 56, 1600.

[2] G. M. J. Barca, C. Bertoni, L. Carrington, D. Datta, N. De Silva, J. E. Deustua, D. G. Fedorov, J. R. Gour, A. O. Gunina, E. Guidez, T. Harville, S. Irle, J. Ivanic, K. Kowalski, S. S. Leang, H. Li, W. Li, J. J. Lutz, I. Magoulas, J. Mato, V. Mironov, H. Nakata, B. Q. Pham, P. Piecuch, D. Poole, S. R. Pruitt, A. P. Rendell, L. B. Roskop, K. Ruedenberg, T. Sattasathuchana, M. W. Schmidt, J. Shen, L. Slipchenko, M. Sosonkina, V. Sundriyal, A. Tiwari, J. L. Galvez Vallejo, B. Westheimer, M. Wloch, P. Xu, F. Zahariev, M. S. Gordon, *J Chem Phys* **2020**, 152, 154102.

[3] J. VandeVondele, M. Krack, F. Mohamed, M. Parrinello, T. Chassaing, J. Hutter, *Comput Phys Commun* **2005**, 167, 103.

[4] G. Lippert, J. Hutter, M. Parrinello, *Theor Chem Acc* **1999**, 103, 124.

[5] C. Hartwigsen, S. Goedecker, J. Hutter, *Phys Rev B* **1998**, 58, 3641.

[6] M. T. S. Goedecker, J. Hutter, *Phys Rev B* **1995**, 54, 1703.

[7] M. C. o. e. Bernd G. Pfrommer, Steven G. Louie, and Marvin L. Cohen, *J Comput Phys* **1998**, 131, 233.

[8] R. Sassi, R. R. Bond, A. Cairns, D. D. Finlay, D. Guldenring, G. Libretti, L. Isola, M. Vaglio, R. Poeta, M. Campana, C. Cuccia, F. Badilini, *J Electrocardiol* **2017**, 50, 776.

[9] S. Reis-Dennis, *Monash Bioeth Rev* **2020**, 38, 83.

[10] S. Grimme, S. Ehrlich, L. Goerigk, *J Comput Chem* **2011**, 32, 1456.

[11] A. D. Becke, *J Chem Phys* **1993**, 98, 5648.

[12] M. H.-G. So Hirata, *Chemical Physics Letters* **1999**, 314, 291.

[13] A. S. Hehn, B. Sertcan, F. Belleflamme, S. K. Chulkov, M. B. Watkins, J. Hutter, *J Chem Theory Comput* **2022**, 18, 4186.

[14] J. Strand, S. K. Chulkov, M. B. Watkins, A. L. Shluger, *J Chem Phys* **2019**, 150, 044702.

[15] Giovanni Bussi, Davide Donadio, a. M. Parrinello, *J Chem Phys* **2007**, 126, 014101.

[16] W. Kong, W. Liu, X. Zheng, Q. Xu, *Adv Optical Mater* **2023**, 2301821.

[17] C. Zhu, P. Liu, B. Niu, Y. Liu, W. Xin, W. Chen, X. Y. Kong, Z. Zhang, L. Jiang, L. Wen, *J Am Chem Soc* **2021**, 143, 1932.

[18] Z. Zhang, S. Yang, P. Zhang, J. Zhang, G. Chen, X. Feng, *Nat Commun* **2019**, 10, 2920.

[19] Z. Zhang, X. Sui, P. Li, G. Xie, X. Y. Kong, K. Xiao, L. Gao, L. Wen, L. Jiang, *J Am Chem Soc* **2017**, 139, 8905.

[20] Z. Zhang, X. Y. Kong, K. Xiao, Q. Liu, G. Xie, P. Li, J. Ma, Y. Tian, L. Wen, L. Jiang, *J Am Chem Soc* **2015**, 137, 14765.

[21] Y. Wu, W. Xin, X.-Y. Kong, J. Chen, Y. Qian, Y. Sun, X. Zhao, W. Chen, L. Jiang, L. Wen, *Mater Horiz* **2020**, 7, 2702.

[22] Q. Wang, Y. Wu, C. Zhu, Y. Hu, L. Fu, Y. Qian, Z. H. Zhang, T. Li, X. Li, X. Y. Kong, L. Jiang, Z. Zhang, L. Wen, *Angew Chem Int Ed Engl* **2023**, 62, e202302938.

[23] Q. Luo, P. Liu, L. Fu, Y. Hu, L. Yang, W. Wu, X. Y. Kong, L. Jiang, L. Wen, *ACS Appl Mater Interfaces* **2022**, 14, 13223.

[24] X. Lin, P. Liu, W. Xin, Y. Teng, J. Chen, Y. Wu, Y. Zhao, X. Y. Kong, L. Jiang, L. Wen, *Adv Funct Mater* **2021**, 31, 2105013.

[25] J. Ji, Q. Kang, Y. Zhou, Y. Feng, X. Chen, J. Yuan, W. Guo, Y. Wei, L. Jiang, *Adv Funct Mater* **2016**, 27, 1603623.

[26] K. T. Huang, W. H. Hung, Y. C. Su, F. C. Tang, L. D. Linh, C. J. Huang, L. H. Yeh, *Adv Funct Mater* **2023**, 33, 2211316.